# OXIDATION BEHAVIOR OF COMPLEX NIOBIUM BASED ALLOYS

E. Sarath K Menon [(1)], Madan G. Mendiratta [(1)] and Dennis M. Dimiduk[(2)]

(1) UES Inc., 4401 Dayton-Xenia Road, Dayton, OH 45432-1894, USA.
(2) Air Force Research Laboratory, Materials and Manufacturing Directorate, AFRL/MLLM, Wright-Patterson Air Force Base, OH 45433-7817, USA.

**Abstract**

This paper begins by examining the general physical metallurgy of complex Nb based alloys that are potentially useful in high-temperature applications. The focus of the paper is on the nature of high-temperature oxidation resistance in these alloys and the effect of alloying on the microstructure and related improvements in oxidation behavior of Nb-Ti-Si base alloys. The general features associated with the oxidation reactions at various temperatures for Nb alloys have been investigated with emphasis on the role of different alloying elements. In particular, the overall kinetics of the oxidation reaction, the nature of the reaction products and the development of the oxidation products have been thoroughly evaluated and the mechanism of oxidation discussed briefly.

## Introduction

Niobium alloys have attracted the attention of researchers as a potential new generation of refractory material system that could meet the high-temperature capability envisaged to exceed the application temperatures of Ni base superalloys. Indeed, selected use of niobium and its alloys have been made in a variety of areas such as in aircraft, nuclear and space industries. Detailed reviews of earlier work on Nb alloys can be found in several publications such as (1-4). Currently, research on a new generation of Nb- based multicomponent alloys having a balance of high-temperature mechanical properties and good oxidation resistance is actively being pursued by many workers (5-10). However, one of the main concerns in the application of Nb based alloys is their poor oxidation resistance at elevated temperatures (9), and a protective coating maybe necessary. Alloying of the Nb solid-solution has been shown to be quite effective in obtaining remarkably improved high-temperature oxidation resistance without compromising other high-temperature mechanical properties (5, 7-9). Alloy systems containing high volume fractions of the high-melting intermetallic silicide phase together with the ductile refractory solid-solution have been investigated in detail because they offer the potential of developing high-temperature structural materials (5, 7-9). Thus, Nb-Ti alloys containing Si as the main ternary alloying addition, together with other elements such as Cr, Al and Hf, have been investigated (5,11). Multi-phase complex alloys containing an appropriate mixture of the bcc solid-solution phase, $Nb_5Si_3$ type silicide phase, $Ti_5Si_3$ type silicide phase and Laves phase have been examined (11). All of these studies were carried out as part of an alloy development program having emphasis on improving the mechanical behavior of alloys and checking the oxidation resistance of promising alloys. Detailed reviews of all recent studies and evaluations of mechanical behavior of advanced Nb-based intermetallics have been published (5-11) and a summary of our efforts is outlined in a later section. This review will instead focus on recent results regarding the oxidation behavior of several complex alloys.

Extensive investigations aimed at achieving oxidation-resistant Nb alloys have indeed been carried out in the past and serve as useful guidelines in the recent alloy-development studies (12-14). Most of these efforts were based on the development of Nb-Al alloys, and the formation of marginally protective alumina scales at high-temperatures was reported for some complex alloys (14-16). The recent alloy-development efforts have focussed on the promising potential of silicide-bearing multicomponent Nb alloys, and this study was initiated to examine the oxidation behavior of this class of Nb alloys. Silica can, in principle, provide a stable surface oxide to higher temperatures than alumina and the lower activation energy for oxygen diffusion in silica may make it more effective than alumina at higher temperatures (14). Since other major alloying additions in promising Nb alloys include elements such as Ti, Al and Hf, all of which form oxides that are even more thermodynamically stable than silica, and since $SiO_2$ and $Nb_2O_5$ have virtually no solubility in the solid state, complex oxide scale formation is expected to occur during oxidation of the multicomponent Nb alloys. A crucial drawback is the fact that the binary phase diagrams for these oxides with $Nb_2O_5$ (melting point ~ 1550° C) indicate eutectic formation (2, 17) and thus the maximum useful or safe temperatures before catastrophic melting of the oxide scales may be further lowered.

Thus, it is important that a fundamental understanding of the influence of chemistry and microstructure on the nature, sequences and mechanisms of oxidation at various temperatures be gathered. We have recently examined the kinetics of oxidation of advanced Nb-Ti-Si based

alloys (18) and thus, in this paper only the general mechanism of oxidation of these alloys at various temperatures will be discussed.

Physical Metallurgy of Complex Nb Base Alloys

Many of the Nb alloys under consideration contain a mixture of the ductile β solid-solution phase and several intermetallic phases depending upon the alloying elements. Most of the alloying elements such as Ti, Cr etc. act as both solid-solution strengtheners as well as compound formers. Detailed characterization of Nb-Ti-Al alloys have been published in the literature (19-22) are not discussed here. Microstructural developments and correlation with mechanical properties of several Nb-Si alloys have also been published in recent years (23-26). Instead attention is focussed on the microstructures of Nb-Ti-Si base alloys. During casting the Si-bearing alloys go through a complex solidification sequence starting with the formation of the $Nb_5Si_3$ – type phase and subsequent solid-state precipitation of other intermetallic phases such as a $Ti_5Si_3$ – type silicide and the $Cr_2Nb$ – type Laves phase. As an example, the microstructures of two alloys are compared in Figure 1. The microstructure contains a distribution of the $Nb_5Si_3$ type phase in a solid-solution matrix, the β phase. XRD analysis showed that in all the Ge-containing alloys, it was the high-temperature form of the silicide phase, designated as the β - $Nb_5Si_3$ type phase having a $D8_m$ crystal structure with c/a ~ 0.5, that was stabilized to room temperature after the heat treatment employed here. Only in alloys without any Ge was the α - $Nb_5Si_3$ type phase having a $D8_l$ crystal structure with c/a ~ 1.8 found. In all the alloys, formation of another silicide phase designated as the $Ti_5Si_3$ type phase was also observed. This phase was usually found at the β / $Nb_5Si_3$ type phase boundaries as indicated by arrows in Figure 1, and was determined by XRD to be isostructural with the hexagonal $Ti_5Si_3$ structure. The two alloys compared in Figure 1 differ most notably in their Cr and Si contents but similar heat treatments generate significant differences in their microstructural constituents. Most importantly, the slight increase of Cr in the alloy brought it into a phase field where the $Cr_2Nb$ – type phase was also stable. The presence of the Laves phase can indeed lead to considerable differences in the mechanical behavior of the alloy. Table I compares the compositions of the individual phases as determined by microprobe analysis. A careful examination of the composition of the constituent phases reveals that the chemistry of the common phases in the two alloys are quite similar.

Table I Experimentally determined compositions (in atomic %) of the various phases

| **At. %** | b | **$Nb_5Si_3$ -type** | | **$Ti_5Si_3$ -type** | | **$Cr_2Nb$ -type** |
|---|---|---|---|---|---|---|
| | Fig 1(a) | Fig. 1(b) | Fig. 1(a) | Fig. 1(b) | Fig. 1(a) | Fig. 1(b) | Fig. 1(a) |
| Nb | 53.07 | 57.99 | 38.04 | 38.59 | 28.28 | 26.80 | 21.78 |
| Ti | 30.23 | 26.58 | 18.04 | 22.23 | 26.22 | 29.18 | 12.65 |
| Si | 0.45 | 0.50 | 30.83 | 25.78 | 27.67 | 26.47 | 6.05 |
| Ge | 0.16 | 0.06 | 5.72 | 7.34 | 7.80 | 9.19 | 0.34 |
| Hf | 1.03 | 0.72 | 4.74 | 1.71 | 6.73 | 6.10 | 4.74 |
| Al | 3.35 | 2.60 | 1.19 | 1.54 | 2.13 | 1.22 | 0.98 |
| Cr | 11.72 | 10.06 | 1.43 | 2.41 | 1.17 | 0.90 | 54.81 |
| Sn | - | 1.51 | - | 0.41 | - | 0.14 | - |

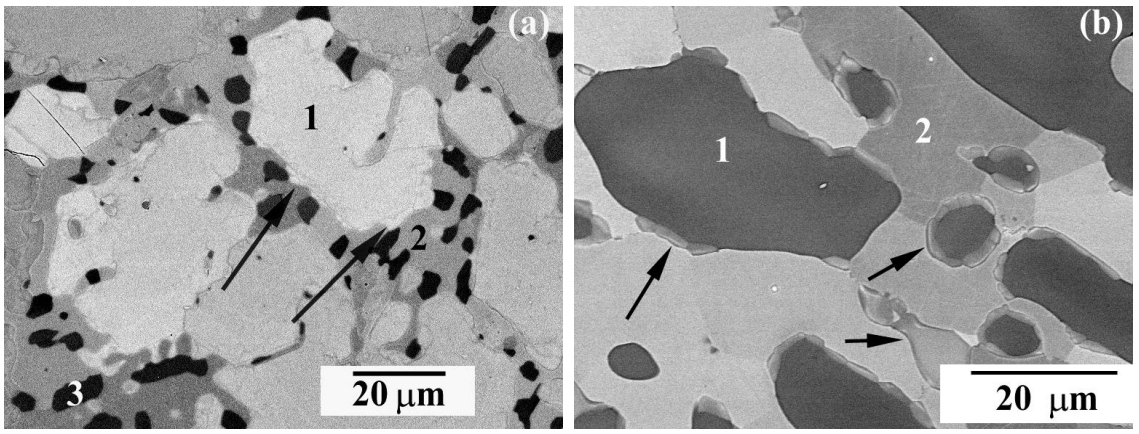


Figure 1: Microstructure of two alloys homogenized and heat treated at 1200°C (a) Nb-19.86Ti-19.74Si-4.21Ge-3.26Al-4.21Hf-9.90Cr and (b) Nb-25.99Ti-12.61Si-4.94Ge-1.92Al-1.90Hf-6.73Cr-0.43Sn. In these micrographs 1 denotes the $Nb_5Si_3$ – type phase, 2 the b phase and the arrows point to the $Ti_5Si_3$ – type phase. The dark phase denoted as 3 in (a) is the Cr rich Laves phase.

Comparison of the microprobe results from alloys heat treated at different temperatures (up to 800°C) showed that there was only very small changes in the compositions of the phases as a function of the temperature. The following observations could be made from the microprobe analyses on heat-treated homogenized alloys: (a) In general, the equilibrium compositions of the phases varied only slightly between the two heat-treatment temperatures suggesting that the phase boundaries are quite steep in this region of the multicomponent phase diagram. (b) The solubility of Si as well as Ge in the solid-solution is very low while a substantial amount of Cr and most of the Sn remains in the solid-solution. (c) The two silicides may be easily distinguished from their compositions as the $Nb_5Si_3$ and the $Ti_5Si_3$ type phases, and these are associated with Nb/Ti atomic ratios of approximately 1.8-2.0 and 0.8-0.9, respectively. (d) Both of the silicides are enriched in Ge, presumably substituting for Si in their crystal structures, while Hf clearly shows preferential partitioning into the $Ti_5Si_3$ type phase. These experimental observations are in conformity with expected alloying behavior based on their binary phase diagrams. (e) The maximum solubility of Cr in the β phase is close to 10-11at% and as the alloy composition approached this limit, the tendency for Laves phase to appear as an equilibrium phase also increased. In fact, replacing half the Cr in the alloy shown in Fig. 1(b) with Fe appeared to lead to a small amount of Laves phase in the resulting alloy. These considerations clearly demonstrate that the microstructures produced in these multicomponent alloys are very strongly dependent on the alloy chemistry, and even a slight change in the average chemistry could lead to drastic microstructural changes. Thus, extreme care is required in the control of chemistry during Nb alloy processing.

Another interesting feature in the microstructures is the presence of the Ti-rich silicide, a $Ti_5Si_3$ type phase. As mentioned before, this phase differs from the $Nb_5Si_3$ type phase in the Nb/Ti ratio and also possesses a hexagonal structure in contrast to the tetragonal $Nb_5Si_3$ type phase. The differences in the chemistry of this phase can easily be seen from the X-ray images shown in Figure 2. The β solid-solution phase is enriched in Cr as well as Al, both of which partition mostly to this phase. The solid solubility of Si in the β phase is low in the alloys considered here (compared to less than 0.1% at 1200°C in the binary equilibrium diagram) and though that of Ge in the Nb-Ge system is much higher, at ~4at% at 1200°C, the solubility of Ge in the

multicomponent system appears to have decreased significantly (see Table I also). Most of the Ge appears to partition exclusively to the silicide phases with the Ti-rich silicide containing a higher amount. As can be seen from these images, the Ti-rich silicide is enriched in Hf as well and the consequence of this upon internal oxidation will be discussed later. From the morphology, it appears that the $Ti_5Si_3$ precipitation results from a solid-state reaction between β and the $Nb_5Si_3$ phases.

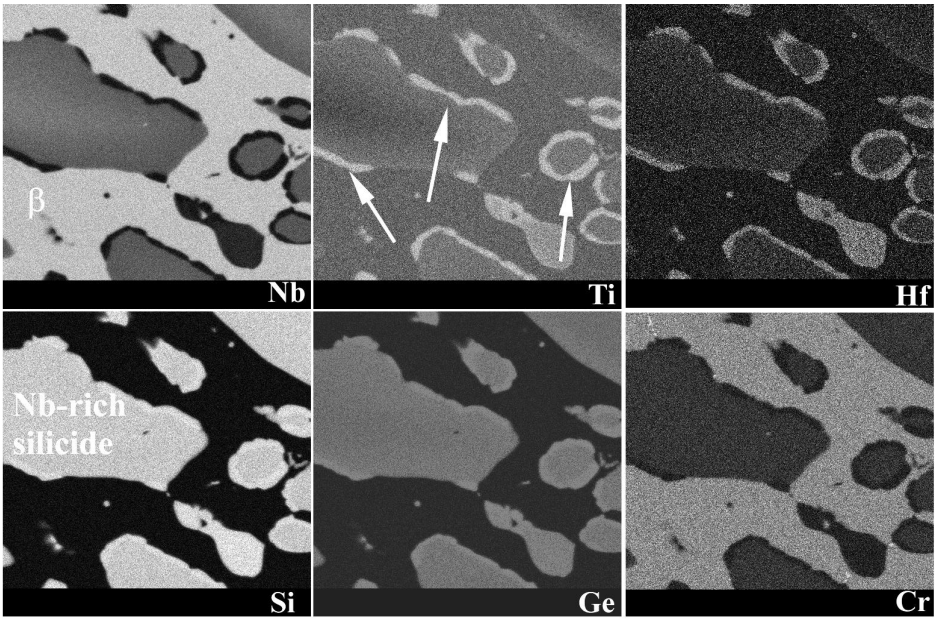


Figure 2: X-ray maps from Nb-25.99Ti-12.61Si-4.94Ge-1.92Al-1.90Hf-6.73Cr-0.43Sn heat treaed at 1200°C for 5 days in inert atmosphere indicating the partitioning of elements among the equilibrium phases. Notice the Ti and Hf enrichment in the silicide that forms at β/$Nb_5Si_3$ the interface.

Kinetics of Oxidation

Oxidation kinetics of several multicomponent alloys were studied in the temperature range 1200° - 800°C for a wide variety of alloys. Figure 3 shows examples of the weight change per unit area for several alloys, plotted against the time of oxidation at 1000°C.

The following observations could be deduced from Figure 3 and similar data at other temperatures.

1. All alloys show a two-stage oxidation reaction with an initial weight gain region followed by a rapid weight loss region. The second stage can be described as a breakaway oxidation reaction where rapid oxidation and oxide spallation occurs. The onset of the breakaway oxidation is strongly temperature dependent and occurs earlier in time as the temperature is raised.
2. Replacement of Si with 5at% Ge appears to have a remarkable favorable influence on the onset of breakaway oxidation, which is delayed by at least an order of magnitude in time. The alloy containing Ge appears to fare the best in comparison to others. Other alloys based on

this composition and containing more Si and small amounts of Ce appeared to behave in a similar fashion.

3. Comparing Fe containing alloys, it seems that replacement of Cr with Fe, or adding B may have a detrimental effect in oxidation resistance. The oxide scales in the latter two alloys tend to break up into fine powder rather than stay as a compact sheet as in other alloys. The positive effect of Ge appears to be somewhat lost when a portion of the Cr is replaced with Fe.

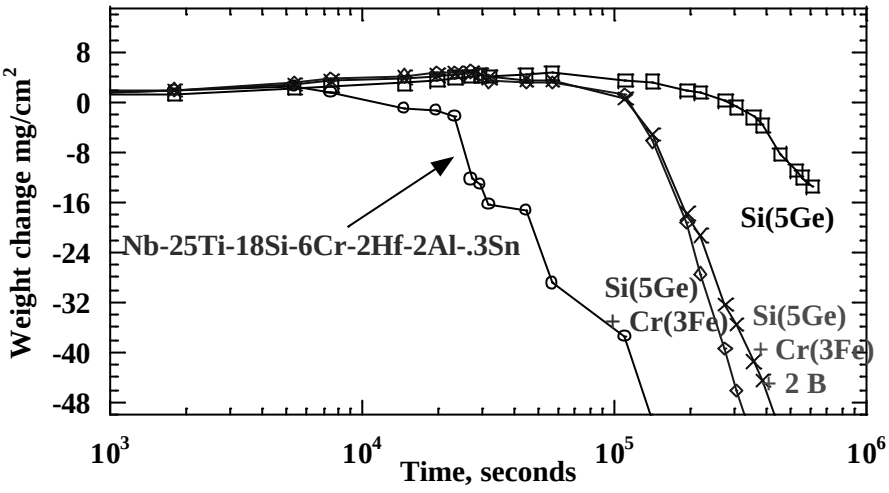


Figure 3: Plots of weight loss during oxidation of Nb - based alloys at 1000°C. Four alloys are compared here. Partial alloy replacements are indicated to compare the effects of alloying on oxidation resistance.

Results of weight change data such as those reported here are usually analyzed by using the equation:

$$\ln (\Delta w) = \ln K + n \ln t \qquad (1)$$

where $Dw$ is the weight change per unit area, $t$ is the reaction time; $K$ and $n$ are constants. The oxidation reaction kinetics is then characterized as linear, parabolic, cubic, etc. depending upon the value of the exponent $n$. Wagner showed that the kinetics of oxidation can be treated as a diffusion problem and a simple parabolic law (i.e. $n = 0.5$ in equation (1)) derived to explain the kinetics of the reaction (27, 28). The oxidation of pure Nb in oxygen (at partial pressures high enough to form $Nb_2O_5$), as well as static air, follows a parabolic law at short times (i.e. $n = 0.5$) and becomes linear at longer exposure times. All the available data from Nb-Al alloys with several complex multicomponent additions have indicated faster than parabolic kinetics with $n > 0.5$ (13, 14). The results of weight changes in Nb-Ti-Si alloys were analyzed according to equation (1). It was found that in general, $n < 0.5$ for all the alloys. Another interesting observation was that Ce-modified alloys showed near-parabolic oxidation kinetics for a considerably longer time at temperatures $\geq 1100°C$. Rhodin (11) has reported in his US patent that excellent oxide-scale adherence could be obtained in Nb-Al-Cr alloys by addition of Ce. The oxidation kinetics of Si-containing, multicomponent Nb alloys appear to be somewhat different from those that are Al rich in the sense that, in Nb-Al based alloys, the value of $n$ was found to be

usually very close to unity (13, 14) indicating much faster oxidation kinetics. This is best seen in Figure 4 where the value of the kinetic law exponent, *n*, in equation (1) is indicated. Included in this figure are the data from Perkins, Chiang and Meier study (13) where several alloys having the composition (25-40) at% Nb- (23-32) at% Ti – (22-44) at% Al with other additions were employed. It must be cautioned that in the cyclic-oxidation experiments performed here, weight changes reported do not account for any weight losses due to spallation and thus the value of the exponent *n* in the kinetic law deduced from these data may actually be somewhat less than the true parameter.

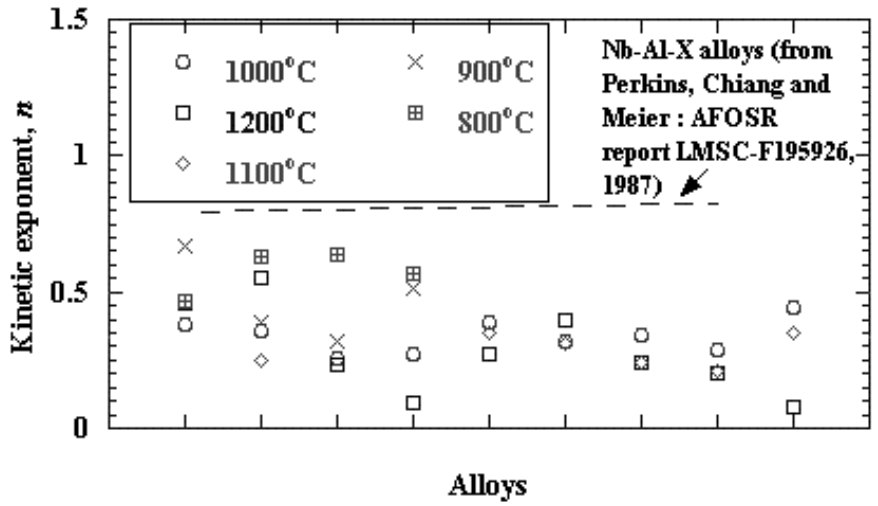


Figure 4: Compilation of experimentally determined values of the kinetic exponent, n for a number of multicomponent Nb base alloys. The average value of n for alloys from Perkins, Chiang and Meier (13) is shown as a dashed line. The rest of the data are from the present work, each symbol denoting data from a particular oxidation temperature.

Examination of Figure 4 clearly shows that the time dependence of oxidation (or the rate of oxidation) for high Si-bearing Nb alloys is less than that of Al-rich Nb-base alloys. While analyzing the oxidation kinetics data in the light of Wagner theory for high-temperature oxidation, one must bear in mind that the assumption of thermodynamic equilibrium at the metal / oxide interface is not realized. This is especially true during oxidation of transition elements belonging to groups IVA (Ti, Zr, Hf) and group VA (V, Nb and Ta) since the solubility of oxygen in these metals is high at high-temperatures (29). Oxygen solubility in Nb is substantial at these temperatures and may be influential in determining the oxidation resistance of multicomponent Nb alloys as well. Thus, in reality, the reaction-rate constant, *K*, in equation (1) represents the sum of reaction rates associated with the dissolution of oxygen in the alloy and the growth of an oxide on the surface of the alloy. One must also bear in mind that the derivation of the parabolic law for oxide growth is based on volume diffusion of oxygen through the oxide while it is certainly possible that short-circuit diffusion could play a significant role in cases like the one in this study. For these the microstructure of the oxide film offers sufficient heterogeneities (as described later) and oxide cracking as well as spallation occurs, such that oxygen maybe transported to the metal-oxide interface at much higher rates than that afforded by volume diffusion alone. Further, if oxygen diffusion in the alloy occurs to appreciable levels, internal oxidation is likely to occur since elements like Hf, Al, Cr that have high affinity for oxygen are

also present in the alloy. Indeed, cubic rate equations described with $n = 1/3$ have been reported in several materials, notably in pure Zr, though parabolic and linear rates describe the oxidation kinetics of Ta and Nb (27, 29). In order to obtain a generalized idea of the type of oxidation reaction mechanism(s) that maybe operative in the fairly wide temperature range employed in this study, the parabolic reaction rate constants, $K_p$, for oxidation of all alloys at different temperatures were calculated from all the data and the Arrhenius-type plot drawn for one of the alloys is presented in Figure 5.

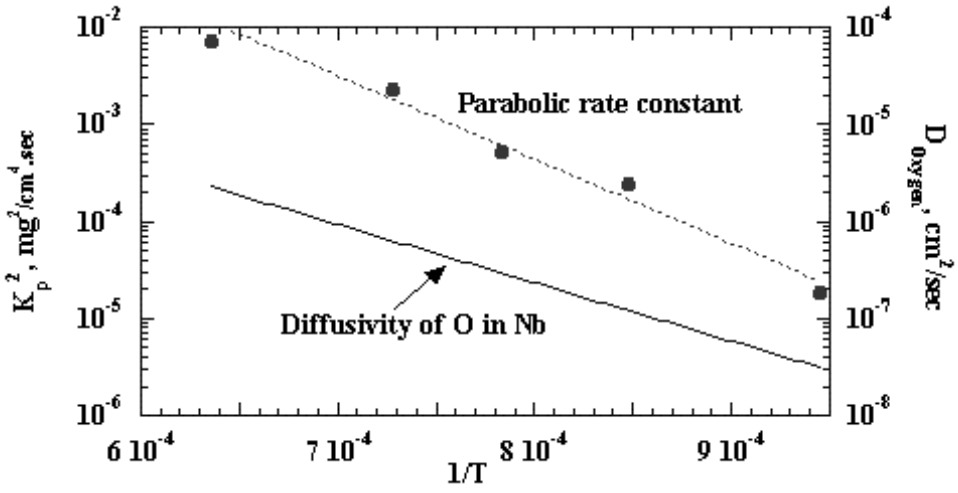


Figure 5: Arrhenius plot showing that the parabolic rate constant, $K_p$, evaluated for oxidation kinetics of a Nb-25.99Ti-12.61Si-4.94Ge-1.92Al-1.90Hf-6.73Cr-0.43Sn alloy varies linearly with the reciprocal of temperature, T, expressed in K. Here, $K_p^2$, mg$^2$/cm$^4$.sec, is plotted against 1/T to compare with $D_{Oxygen}$, the diffusivity of oxygen in Nb (29) shown by the full line.

The data in Figure 5 are clearly linear, indicating that a single mechanism is operative in the entire temperature range of our investigation. By comparing with the diffusivity data of oxygen in pure Nb at these temperatures (29) it was noticed that the activation energy associated with the overall reaction process is approximately 44% higher than that for oxygen diffusion in pure Nb. This is reasonable and it is suggestive of the fact that the alloying elements substantially decrease the diffusivity of oxygen in the Nb solid-solution phase. As an example, it is reported that addition of 25at% Ti to Nb decreases the diffusivity of oxygen by a factor of twenty (2). This data also re-iterates the earlier suggestion that oxygen dissolution in the Nb-rich solid-solution maybe quite significant and substantially affects the kinetics of oxidation of these Nb-base alloys. This is further confirmed from microstructural observations and measurements of compositions in the microprobe.

Structure of the Oxidation Products

The structure of the oxides formed on the surface during oxidation was deduced from X-ray diffraction conducted on oxidized alloys as well as from the spallation products. Details of the products of internal oxidation are discussed in the next section. All the samples yielded virtually the same diffraction pattern irrespective of the oxidation temperature and alloy composition. All

the diffraction peaks from these patterns could be indexed and the samples identified as a mixture of the phases $TiNb_2O_7$ (PDF # 39-1407), $AlNb_{11}O_{29}$ (PDF # 22-0009) and $CrNbO_4$ (PDF # 34-0366) and some $SiO_2$ (PDF # 39-1425, crystobalite). The amount of the various phases did, of course, vary from sample to sample with $SiO_2$ invariably being the minor phase mostly occuring in alloys oxidized at higher temperatures. It is very difficult to quantitatively assess the oxidation products since spallation from different samples made it impossible to ascertain the homogeneity of the collected oxide, and no attempt was made to obtain any quantitative comparison of the oxidation products. Instead, attention was focussed only on the identity of the oxidation products. Though a detailed characterization of oxidation products from multicomponent Nb-based alloys are not available in literature, characterization of the oxidation products from several binary and ternary Nb alloys containing Ti, Al, Si, Cr etc. have reviewed by Samarin (2). The results of the present work are substantially in agreement with results from binary alloys.

Microstructure of Oxidized Alloys

The alloys oxidized at temperatures $\geq 1000^\circ C$ showed similar microstructures. An adherent oxide was always found on the surface of the samples though considerable amounts of oxide scale had been lost due to spallation at long times. Figure 6(a) illustrates the general features associated with oxidation of these alloys. Even in a short period of time, the β phase appears to be severely oxidized though the silicide regions remain virtually unattacked. In Figure 6(a) one can see that roughly ~200μm from the surface of the sample has undergone internal oxidation. This is certainly a great improvement as compared to pure Nb where the diffusion distance for O under identical heat treatment would be ~ 650 μm.

Monitoring the progress of the oxidation of these alloys showed that the oxidation reaction proceeded rapidly to produce a thick oxide scale on the surface of the material. One can also see that the β phase undergoes selective oxidation while the silicide phase virtually remains unaffected. This is in agreement with earlier studies. In his review on the behavior of niobium alloys, Samarin (2) has noted that the $Nb_5Si_3$ phase has much better oxidation resistance than more dilute alloys and that the oxidation resistance of the silicide decreases only above $1100^\circ C$. In addition, it is clear that the $\beta/Nb_5Si_3$ interface undergoes preferential oxidation. A clearer example is shown in Figure 6(b) where one can see that the $\beta/Nb_5Si_3$ interface is decorated with oxide particles. The β-phase regions in this micrograph appear to be well separated into regions of widely differing atomic-number contrast suggesting the presence of different oxides. EDS analysis showed that oxide mixtures of Nb and Ti as well as Cr and Nb were present apart from regions that were almost entirely silica.

Oxidation along the $\beta/Nb_5Si_3$ interface could be seen well inside the sample (for example, middle area in figure 6(a)) where the β grains were relatively free of oxide precipitates. This indicates that phase-boundary precipitation of oxides precedes that within the β-grain interior. In fact, selective formation of various oxides along the $\beta/Nb_5Si_3$ interface, as well as along grain boundaries within the β phase, were always observed. An example is shown in Figure 7. Oxygen penetration into the interior of the sample through the β phase occurs rapidly and leaves a variety of oxide precipitates (as deduced from the different contrast of the precipitates in these back-scattered electron images) within the β grains and at the interfaces. This is understandable since oxides of Al, Si, Ti, Cr and Hf are all thermodynamically more stable than $Nb_2O_5$.

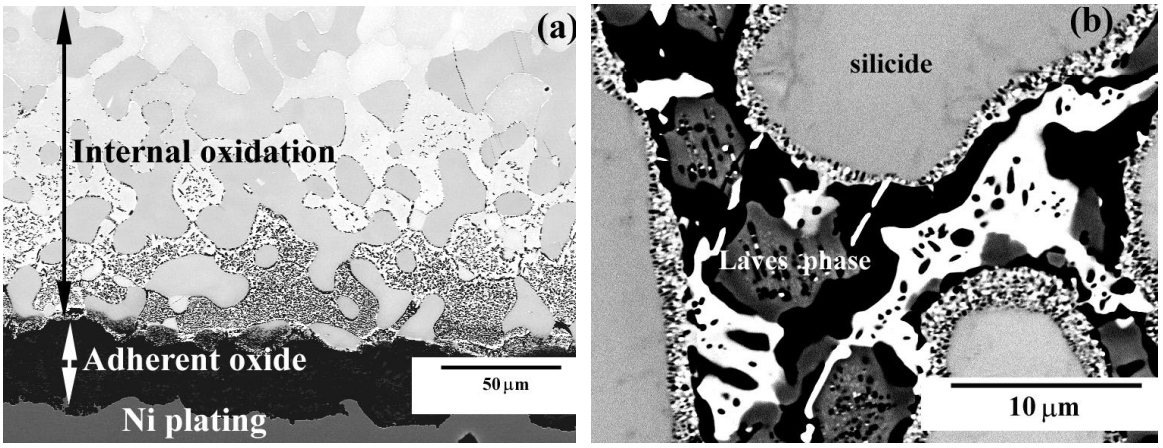


Figure 6: (a) BSE images from Nb-25.99Ti-12.61Si-4.94Ge-1.92Al-1.90Hf-6.73Cr-0.43Sn oxidized at 1200°C for 1 hour Back-Scattered electron images showing the general morphology of the oxide scale and the internal oxidation within the alloy. (b) Nb-19.86Ti-19.74Si-4.21Ge-3.26Al-4.21Hf-9.90Cr oxidized at 1200°C for 48 hours. Notice the variety of oxides (inferred from the strong atomic number contrast in this back-scattered electron image) that are formed at the $\beta/Nb_5Si_3$ interface. Also note that both the β and the Laves phase are internally oxidized.

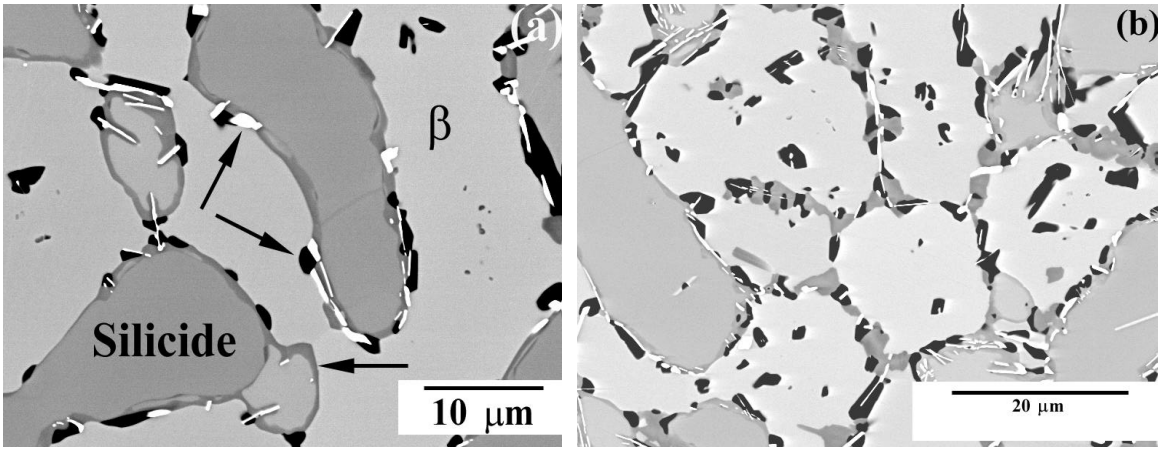


Figure 7: BSE images from alloy 2; oxidized at 1200°C for (a) 24 hours and (b) 48 hours. Images were obtained from well within the sample showing oxide precipitates along the interfaces in the sample. The arrows point out different phases. Various oxides along the grain boundaries of the β phase can be seen in Figure (b).

A high density of brightly imaging precipitates along the phase boundaries can be seen well inside the samples (Figure 7(a)). The fact that these precipitates image as bright particles in the back-scattered images indicate that these are probably Hf rich and this was indeed confirmed by microprobe analysis from some relatively large precipitates and X-ray imaging. The average composition these precipitates was determined by WDS to be 35.34at% Hf-2.42at%Nb-1.18at%Ti-0.47at%Cr-60.62at%O confirming that these are $HfO_2$ particles. Another noteworthy

feature that is vividly illustrated in Figure 7 (b) is the precipitation of oxide phase along the grain boundaries within the β matrix. This indicates that oxygen diffuses rapidly along the internal interfaces in the microstructure (grain boundaries in the β phase as well as the phase boundaries) thus accelerating the oxidation of these alloys. The fact that oxides of different compositions are formed in these materials is clear from the contrast differences easily discerned in Figure 7 (b). Notice that the entire β / silicide boundary area, as well as all the β / β boundaries, are covered by various oxides in these microstructures. Attempts at electron microprobe analysis of these individual oxides were not successful due to the large volume of matrix material from which the x-rays are also excited. However, X-ray images obtained using the EDS detector in the SEM were extremely valuable in identifying these oxides in a qualitative fashion. In addition, the distribution of oxygen along the interfaces further clarified the interpretation of the microstructures. Some examples are shown in Figure 8. One can clearly see the formation of the Ti rich (contains Nb also) oxide along the $\beta/Nb_5Si_3$ interfaces from the Ti and O images. Notice that the Cr rich and the Ti rich areas in these images (an example pointed out by vertical arrows) do not show an overlap, suggesting that these oxides have little solubility in each other as confirmed from their phase diagram. Both these indeed contain Nb as well and are most likely niobates of Cr and Ti, as was the case in the external oxide that was analyzed by XRD. The arrows at 45° angle in the O, Si and Hf images point out the same location in the sample, and at first look, one may infer the precipitate to be a silicate of Hf. However, the Hf-M (1.645eV) and the Si-$K_\alpha$ (1.740) overlap and thus one has to be cautious before the presence of Si is confirmed. WDS analyses confirmed that there was little Si in these rod shaped particles and that they are $HfO_2$.

Examination of the free energy of formation of oxides that can form in these alloys show the trend:

$$\Delta G_{HfO_2} < \Delta G_{Al_2O_3} < \Delta G_{TiO_2} < \Delta G_{SiO_2} < \Delta G_{NbO} < \Delta G_{Cr_2O_3} < \Delta G_{NbO_2} < \Delta G_{Nb_2O_5}$$

Considering the high stability of $HfO_2$ it is easy to understand its formation deep inside the sample. X-ray images clearly show that the $HfO_2$ particles form preferentially at the $\beta/Nb_5Si_3$ interfaces. Comparison of the microstructures and X-ray images of the oxidized samples with those before oxidation (Figures 1 and 2) reveal that preferential internal oxidation of the $Ti_5Si_3$ type phase occurs in these alloys. This is to be contrasted with the nature of the $Nb_5Si_3$ phase that seems to show a high oxidation resistance at high-temperatures. As the compositions of the two silicides in Table I show, though the major difference between the two is in their Nb/Ti ratio and the Hf content, their oxidation resistance is remarkably different. Thus, it is again emphasized that apparent minor differences in alloy chemistry could potentially have major implications in the behavior of these alloys under service conditions.

Segregation of Elements During Oxidation

The distribution of elements across the surface of a Nb-25.99Ti-12.61Si-4.94Ge-6.73Cr-1.90Hf-1.92Al-0.47Sn alloy oxidized at 1200°C is shown in Figure 9. Several features associated with elemental segregation accompanying oxidation reaction are revealed from such experiments.

1. From the oxygen content of the surface oxide, it appears that the major oxide is based on the stochiometry of $Nb_2O_5$.

2. The elements Cr, Si and to some degree Al all appear to have a strong tendency to segregate onto the external surface of the oxide scale.
3. There is a Ge-rich layer below the surface oxide though there is virtually no Ge in the oxide layer.
4. The Nb-rich silicide phase (notice a region just under 100μm from the surface) has little solubility for oxygen.

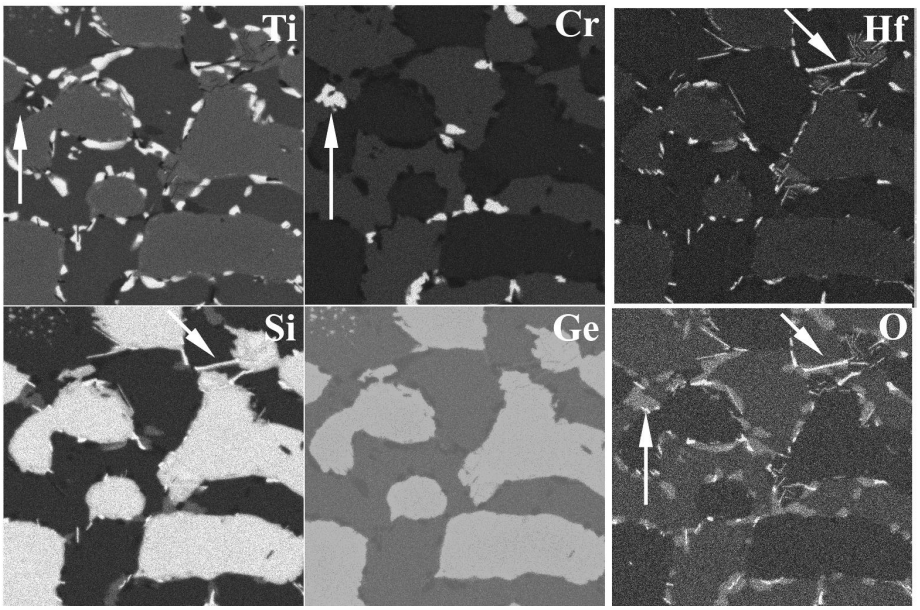


Figure 8: EDS X-ray images from Nb-25.99Ti-12.61Si-4.94Ge-6.73Cr-1.90Hf-1.92Al-0.47Sn oxidized at 1200°C for 1 day. Images obtained from well within the sample showing oxides mostly along the $\beta/Nb_5Si_3$ interfaces. All arrows point out to features that are discussed in detail in the text.

Ge, unlike Si, does not form a highly stable oxide ($?H^{GeO_2} = 129$ Kcal and $?H^{SiO_2} = 210$ Kcal ) and this fact appears to have an impact on the oxidation behavior of the Nb alloys considered here. In fact, it was found that during oxidation at temperatures above ~1000°C, segregation of Ge occurred at regions below the oxide surface and a new phase appeared to grow between the surface oxide and the internally oxidized alloy as shown in Fig. 10(a).

X-ray images obtained from these oxidized samples showed that Ge had segregated to form a layer below the oxide scale. There was no measurable Ge in the oxide in conformity with the fact that the enthalpy of formation associated with Ge oxide was low compared with other elemental oxides from these complex Nb-based alloys. The progress of Ge segregation was monitored by examining the EDS X-ray images shown in Fig. 10(b). Microprobe analysis from samples oxidized for long periods showed that a new phase having the composition, Nb - 18.43at%Ti - 23.23at%Ge - 12.22at%Si - 2.73at%Cr - 2.03at%Hf - 0.91at%Al - 1.92at%Sn, approximately corresponding to a compound of the type $(Nb,Ti)_5(Ge,Si)_3$.

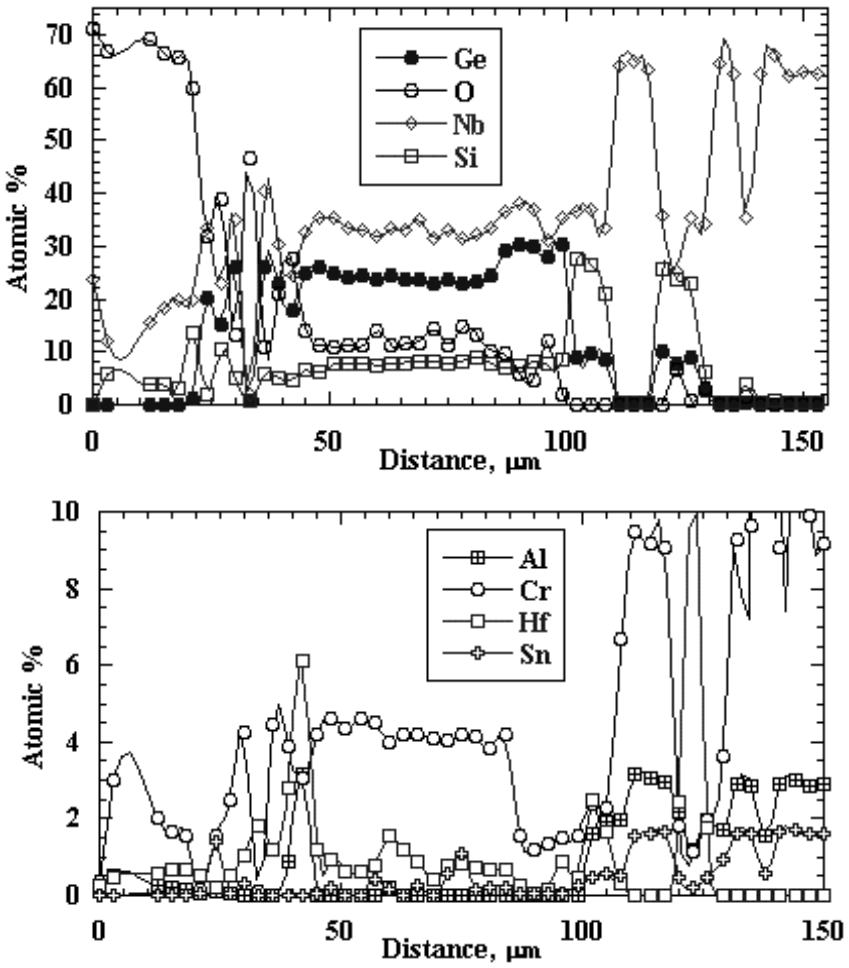


Figure 9: Elemental distribution as determined by WDS across Nb-25.99Ti-12.61Si-4.94Ge-6.73Cr-1.90Hf-1.92Al-0.47Sn oxidized at 1200°C for 134 hours.

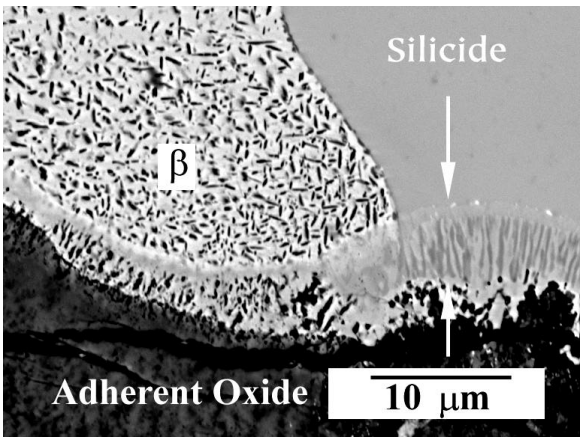


Figure 10(a): Nb-25.99Ti-12.61Si-4.94Ge-6.73Cr-1.90Hf-1.92Al-0.47Sn oxidized at 1100°C for 5 days. Notice the layer between the arrows just below the adherent oxide layer.

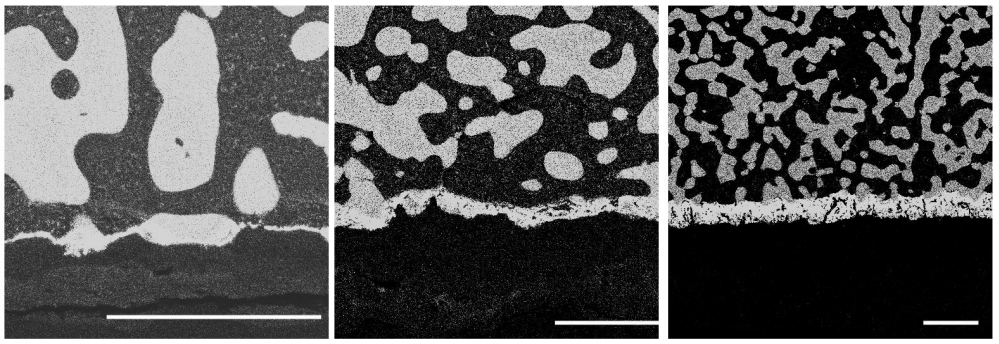

Figure 10(b): Nb-25.99Ti-12.61Si-4.94Ge-6.73Cr-1.90Hf-1.92Al-0.47Sn; Ge-L images from alloy oxidized at 1200°C for 1 hr, 5 hrs and 24 hrs respectively. The micron bar represents 25 μm. Remember that the solubility of Ge in the solid-solution β phase is extremely small and is virtually absent in the oxide layer.

$Nb_5Ge_3$ is an equilibrium phase in the binary Nb-Ge system and has a structure similar to the low temperature form of $Nb_5Si_3$. During oxidation it appears that Ge segregates towards the alloy/oxide interface and the intermetallic phase forms.

Effect of Ce Additions to Oxidation of Nb Alloys

The effect of small additions of Ce on the kinetics of oxidation and also the microstructure of Nb alloys were evaluated. eight-change plots shown in Figure 11 demonstrates that 0.1at% Ce had some important effects on the general oxidation behavior of these alloys. Noticeably, it can be seen that the initial stage of oxidation where equation (1) holds well is prolonged to longer periods especially at temperatures above 1000°C. The kinetic exponent was also found to be always less than those compared to alloys not containing Ce.

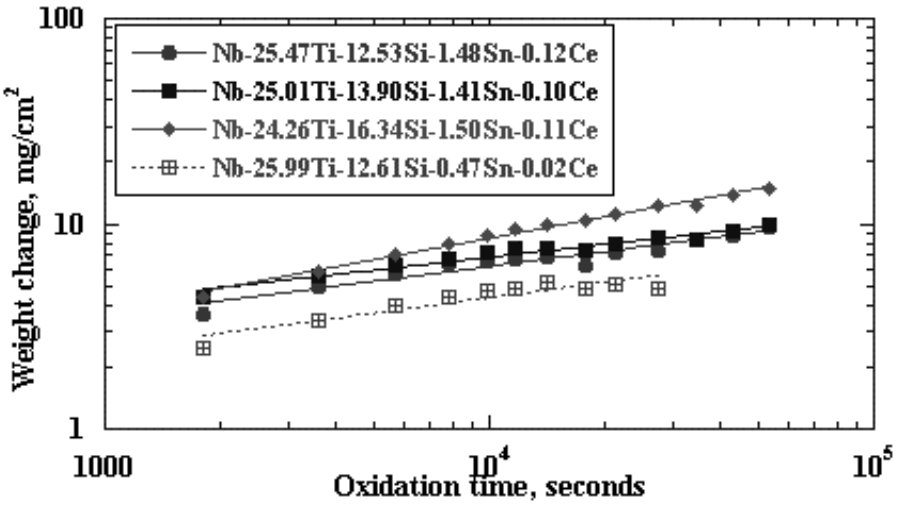


Figure 11: initial stages of oxidation of alloys containing Ce at 1100°C. All these alloys also contained about 5at%Ge-7at%Cr-2at%Hf-2at%Al.

The distribution of the oxide precipitates in the Ce containing alloy appeared somewhat different in the sense that their distribution appeared to be finer within the β phase. This is compared in Figure 12 (a) and (b) where illustrative microstructures of two alloys, one with and other without Ce are shown. The dark and light regions in Figure 12(a) were found to be mostly oxides of Ti and Nb, respectively, while the light regions in Figure 12(b) were the β phase. Even after 48 hours of oxidation, the oxide precipitates in similar locations with respect to the surface are seen to be finer. The presence of $CeO_2$ could not be confirmed in these samples, but they are presumably too fine to be resolved in the SEM level.

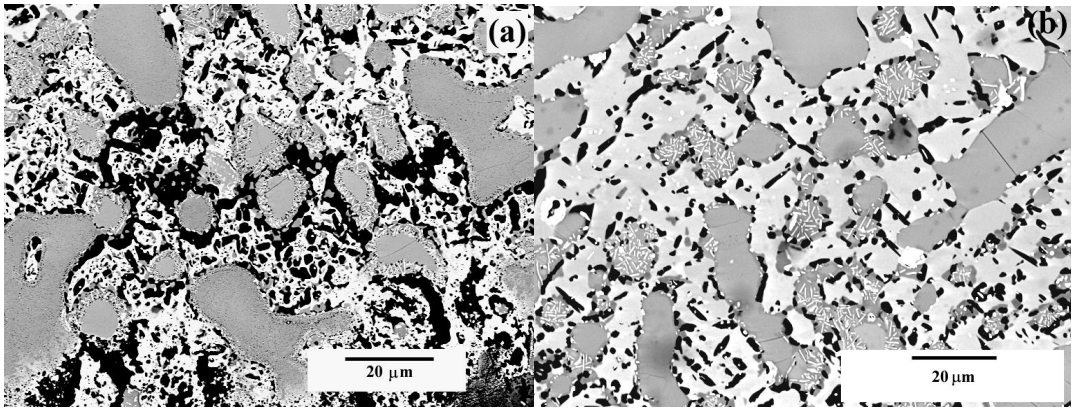


Figure12: (a) Nb-26Ti-13Si-5Ge-7Cr-2Hf-2Al-0,5Sn alloy oxidized at 1200°C for 24 hours and (b) Nb-26Ti-14Si-5Ge-7Cr-2Hf-2Al-1.5Sn-0.1Ce alloy oxidized at 1200°C for 48 hours. Notice the difference in the scale of the microstructure.

Microstructure of the Oxide Scale

The oxidized layer on the surface of these Nb alloys also showed strong back-scattered electron contrast (illustrated in Figure 13) indicating that the oxide layer also remains as a multiphase mixture.

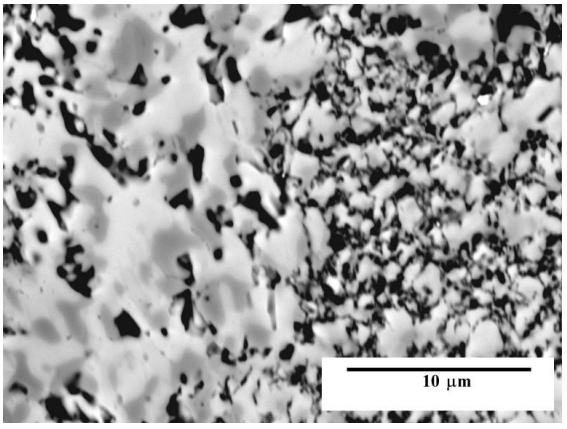


Figure 13: Alloy 2, oxidized at 1200°C for 24 hours. Left is the oxide poorer in the dark appearing Si rich phase while right side that presumably evolved from the silicide has much more of the dark appearing smaller particles.

The dark phase in the oxide layers in all these alloys was identified to be mostly composed of $SiO_2$ while the lighter matrix was found to be a mixture of mostly Ti and Nb oxides. A closer examination clearly showed that at least in the initial stages of the oxidation process, the oxides that evolved from the β phase and the silicide phase were somewhat different.

Obviously, higher density of dark-appearing $SiO_2$ marked the silicide areas while the β phase regions transformed to a mixture of silica and oxides of Cr and/or Ti all of which were distributed in the matrix of Nb oxide. This was best seen from X-ray images obtained from samples during their initial stages of oxidation. Figure 14 shows a series of O, Cr, Nb, Ti and Si images illustrating the development of the oxide. In Figure 14, the "ghost images" of the silicide phase can be clearly seen in the oxide layer (lower one-third of the figure: examine the O-K images) and one can see that the silicide phase has been converted into Nb(Ti) oxide and silica. Comparing these with the Ge-L images in Figure 10(b) it becomes clear that the Ge from the $(Nb,Ti)_5(Si,Ge)_3$ phase did not enter the oxide phase and remained at the alloy/oxide interface eventually forming another phase. Another interesting point that may be noted in the Cr images is that though Cr appeared to have segregated to the surface initially, it mostly remained as internal oxides within the alloy rather than in the oxide scale.

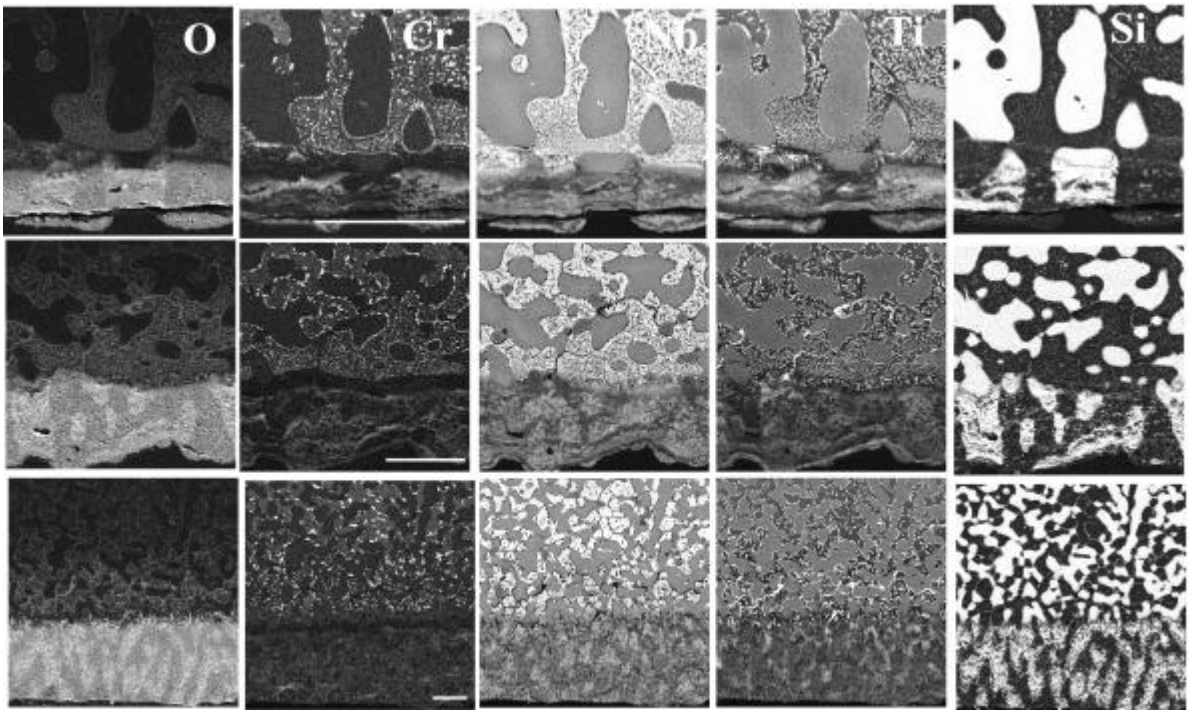


Figure 14: Nb-25.99Ti-12.61Si-4.94Ge-6.73Cr-1.90Hf-1.92Al-0.47Sn; O-K, Cr-K, Nb-L, Ti-K and Si-K images from alloy oxidized at 1200°C for 1 hr, 5 hrs and 24 hrs respectively. The micron bars in the Cr images represent 25 μm. The Ge-L images corresponding to these were shown in Figure 10(b).

Oxidation at Low Temperatures

Weight-change data for most of the alloys at temperatures below 900°C did not show a breakaway oxidation period at least till about 150 hours. Figure 15 shows a log-log plot of the

weight increase observed in many alloys and unlike the data in Figure 3, the rapid weight loss associated with breakaway oxidation is not seen here.

The absence or at least a very long incubation period associated with breakaway oxidation in these alloys at temperatures as high as 900°C is certainly a remarkable improvement over Nb and suggests that the oxidation resistance of these alloys is very much improved by alloying.

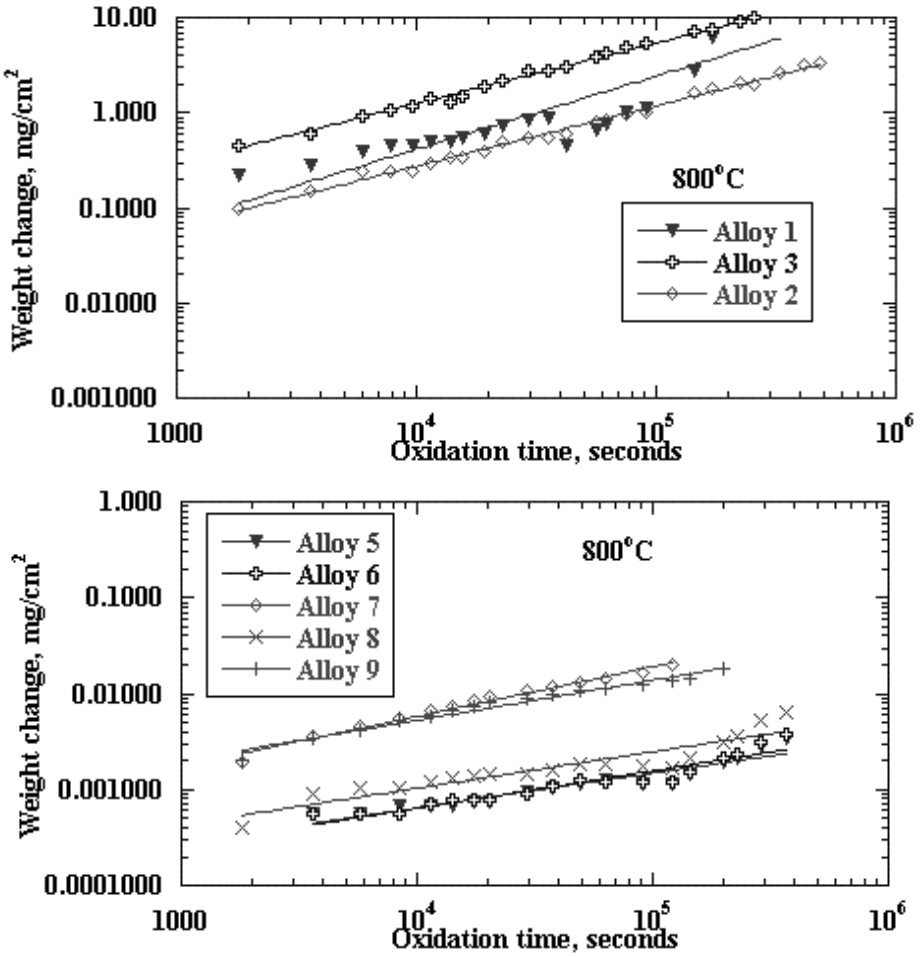


Figure 15: Weight increase during oxidation of a number of Nb alloys at 800°C. Alloy 1 : Nb-24.82Ti-17.62Si-0.17Ge-5.92Cr-1.95Hf-1.89Al-0.32Sn; Alloy 2 : Nb-25.99Ti-12.61Si-4.94Ge-6.73Cr-1.90Hf-1.92Al-0.47Sn; Alloy 3: Nb-25.12Ti-12.96Si-5.48Ge-2.83Cr-2.48Fe-1.98Hf-1.90Al-0.44Sn; Alloy 5: Nb-25.49Ti-14.88Si-4.46Ge-6.13Cr-1.63Hf-1.88Al-1.58Sn; Alloy 6 : Nb-24.64Ti-16.84Si-4.17Ge-6.24Cr-1.37Hf-1.88Al-1.50Sn; Alloy 7: Nb-25.47Ti-12.53Si-4.81Ge-6.64Cr-1.43Hf-1.94Al-1.48Sn-0.12Ce; Alloy 8: Nb-25.01Ti-13.90Si-4.75Ge-6.48Cr-1.39Hf-1.76Al-1.51Sn-0.10Ce; Alloy 9: Nb-24.26Ti-16.34Si-4.86Ge-6.67Cr-1.74Hf-1.84Al-1.50Sn-0.11Ce.

However, a common microstructural observation made in all the alloys that were oxidized at temperatures of 900°C or less was that the surfaces of all the alloys were characterized by cracks parallel to the surfaces just below the oxide layer. This phenomenon of progressive failure of

niobium alloys during low-temperature oxidation has not been reported in the prior literature. This phenomenon is distinct from "pesting" commonly associated with low temperature breakaway oxidation in intermetallic alloys (30). Examples of the microstructures that were observed are shown in Figure 16. From the micrographs shown in Figure 16, one could make the following observations.

1. Small cracks form just below the surface oxide layer (see figure 16(a)) and these cracks appear mostly in the silicide phase, though one can see them in the β phase as well to a lesser extent. There is a considerable amount of oxygen in the β phase as can be seen from the changing contrast in the back-scattered electron images since the oxygen-enriched areas appear darker towards the edge of the sample. (See figure 16(a)). The contrast between the β phase and the silicide seems to have almost reversed itself as the solid-solution phase becomes enriched in oxygen, thus considerably lowering the back-scattered electron yield in these regions.
2. The surface cracks forming in the alloy appear to follow the sample geometry, or in other words the oxygen concentration profile as can be clearly seen from figure 16(b).
3. A closer examination of the β phase in these regions near the oxide/alloy interface showed that fine needle-shaped precipitates (presumably of some oxide phase) had indeed formed within the β matrix. This is illustrated in Figure 16 (c).
4. The surface-cracking phenomenon appears to occur even at low temperatures as illustrated in Figure 16(d) where cracks can be seen to have formed at 600°C.

The surface cracking reported here is indeed associated with oxidation since heat treatment of the same alloys at these temperatures in inert atmosphere did not introduce cracking of the silicide phase, as evidenced from microstructural studies (Figure 17). Also, different cooling rates were employed to ensure that the surface cracking was not the result of thermal stresses induced during cooling.

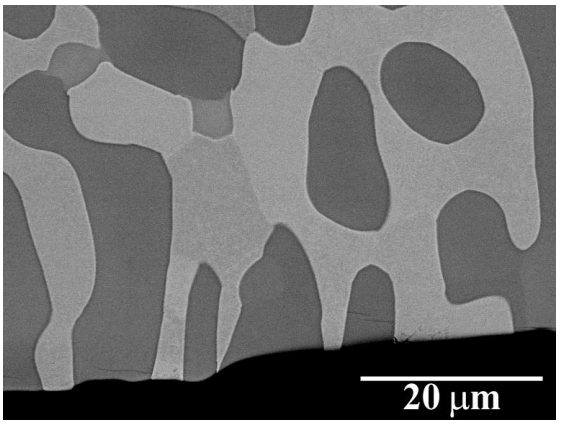


Figure 17: Nb-25.99Ti-12.61Si-4.94Ge-6.73Cr-1.90Hf-1.92Al-0.47Sn, heat treated in Ar atmosphere at 800°C for 72 hours. Notice that the edge of the sample near the mounting material shows no surface cracks in the dark silicide phase.

From these observations, it is clear that somehow, high residual stresses are being developed in the β phase during oxidation, and the silicide that is presumably brittle even at these temperatures

fractures under these stresses. $Nb_2O_5$ has a negative thermal expansion coefficient and fine-scale precipitation of the oxide such as that shown in Fig. 16(c) may lead to generation of residual stresses in the β phase at these temperatures. At higher temperatures, lower thermal-expansion coefficient, together with the ability of the silicide phase to sustain plastic flow prevents fracture of the silicide phase. To test this hypothesis, residual stresses generated during oxidation of polished samples at 800°C were measured from X-ray diffraction experiments.

Figure 18 shows the plot of residual stresses as oxidation progresses, demonstrating that compressive stresses are quickly developed within the β phase during the initial stages of oxidation. Further, it appears that once the stresses reach a critical value, fracture of the brittle phase (silicide) occurs, thus relieving the stresses. SEM examination of the surface of these samples showed that oxide whiskers grew in the β phase (Figure 18) very early during high-temperature exposure to atmosphere.

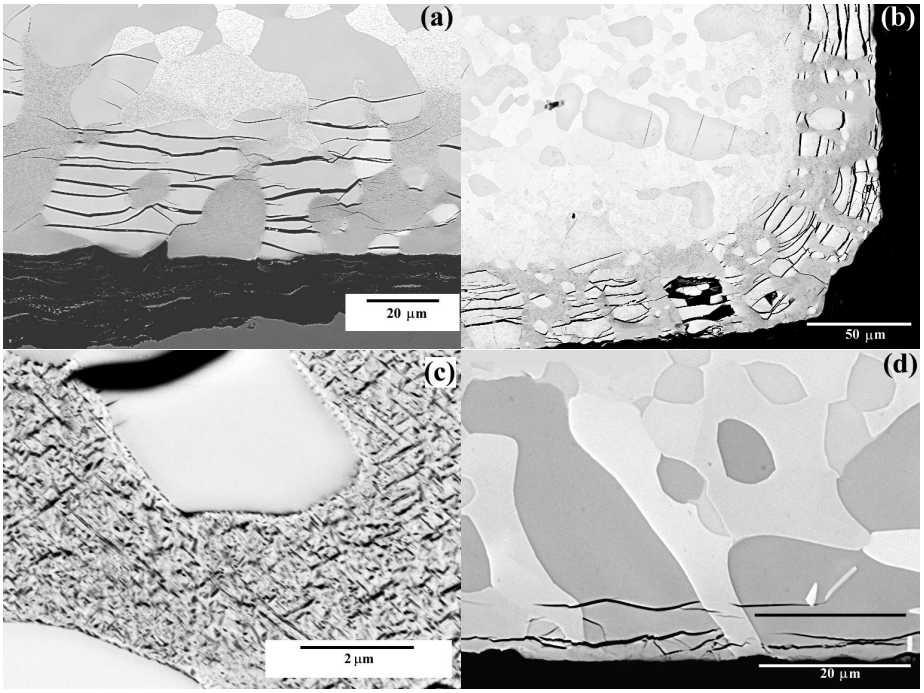


Figure 16: (a) Nb-25.99Ti-12.61Si-4.94Ge-6.73Cr-1.90Hf-1.92Al-0.47Sn, oxidized at 800°C for 150 hours; (b) Nb-25.49Ti-14.88Si-4.46Ge-6.13Cr-1.63Hf-1.88Al-1.58Sn, oxidized at 800°C for 48 hours; (c) Nb-24.26Ti-16.34Si-4.86Ge-6.67Cr-1.74Hf-1.84Al-1.50Sn-0.11Ce, oxidized at 800°C for 48 hours and (d) Nb-25.99Ti-12.61Si-4.94Ge-6.73Cr-1.90Hf-1.92Al-0.47Sn, oxidized at 600°C for 72 hours.

Notice the gradual increase in the intensity within the β phase regions in figure 16(a) from sample interior to the surface while the silicide appears gray throughout. Observe that the cracks follow the contour of the sample as demonstrated in figure 16(b). Fine needle shaped oxide appears to precipitate in the β phase while the silicide appears precipitate free except at the β/ silicide interface where also precipitation can be observed.

From figure 19, it becomes evident that a dense array of needle-shaped oxides form and grow rather quickly in the β phase as compared to the silicide phase. It may also be noted that the β phase appears in relief in this secondary image, indicating that the larger volume of the oxide indeed has left it in a state of considerable compression, in conformity with the residual stress measurements (Figure 19). Surely, as oxygen diffuses deeper in to the sample with longer exposure, oxide precipitation occurs and consequently, β regions inside the sample are stressed to a point when fracture of the silicide phase becomes inevitable.

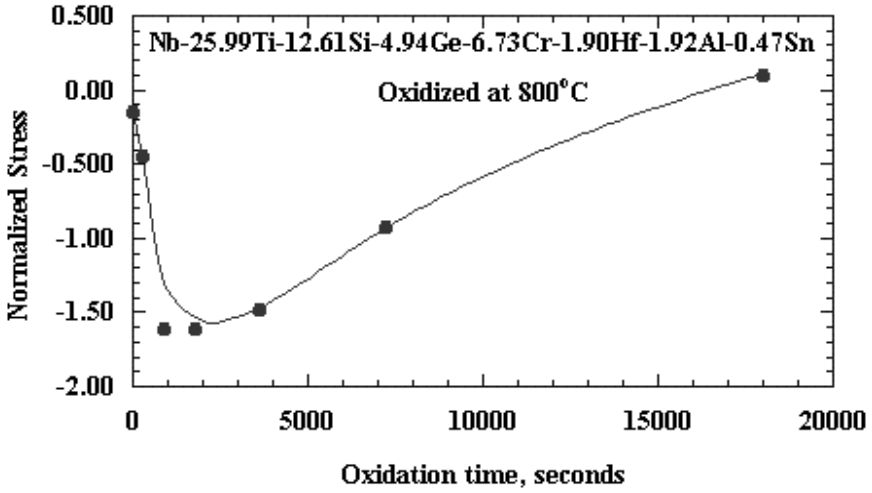


Figure 18: Plot of experimentally determined residual stresses developed in the β phase during oxidation at 800°C. Note that the Y-axis must be multiplied by E/(1+ν) to obtain the actual values of stress.

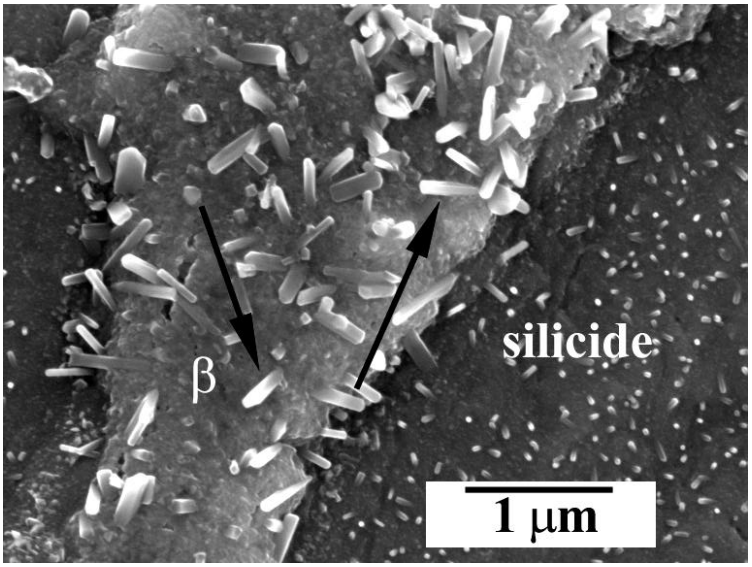


Figure 19: Nb-25.99Ti-12.61Si-4.94Ge-6.73Cr-1.90Hf-1.92Al-0.47Sn, Secondary electron image from the surface of a polished sample oxidized at 800°C for 30 minutes corresponding to ~ the maximum compressive stress developed in the β phase.

This phenomena of surface cracking during low-temperature oxidation of Nb alloys appears to be general and has been observed in a large number of alloys having widely varying chemistry and phase distribution. It is essential that this feature be studied and understood and that steps be taken to alleviate the problem.

In all these studies, the effect of nitrogen has not been evaluated and it must be mentioned here that thermodynamically stable nitrides of major elements such as Nb, Ti etc. present in these complex alloys could have a significant effect on the environmental response of these alloys.

Several strategies of improving the oxidation resistance of powder compacts of Nb alloys are also being pursued (31, 32). Even though significant enhancement of oxidation resistance has been achieved in the complex Nb-based alloys over the commercial Nb alloys, the resistance is still not adequate for hot-section aeroengine structural applications, e.g. for turbine blades. Therefore, an environmental protective coating will be required. It was shown that a commercial coating for Nb alloys (R512E, 20 at% Cr -20 at % Fe -60 at % Si) when applied to the complex Nb based alloys offered significantly enhanced protection to 230 hours at 1200°C under cyclic oxidation conditions. The reliability/durability investigations of this coating and other potential coatings are currently underway (33). Coatings based on aluminides (34) and other quaternary silicides (35) have also been reported.

Mechanical Properties of Complex Nb Base Alloys

The developmental effort on the current multicomponent Nb-based alloys began with the model binary Nb-Si alloys with compositions within the Nb-$Nb_5Si_3$ two-phase field. The effort was based upon the rationale that the intermetallic $Nb_5Si_3$ phase will provide good high-temperature strength and creep resistance while the refractory Nb phase (with Si in solid-solution) will offer fracture resistance via a ductile-phase toughening mechanism. The two-phase Nb/$Nb_5Si_3$ microstructures were found to exhibit excellent thermochemical stability and resistance to coarsening up to 1500°C (23, 24). The mechanical properties of model Nb-rich Nb-Si alloys were investigated (25, 26). The cast + wrought Nb-10 at %Si alloy (75 vol% Nb phase + 25 vol% $Nb_5Si_3$ phase exhibited a room-temperature fracture strength of 828 MPa with very small ductility (~ 0.5%). The brittle-to-ductile transition was found to be ~1000°C with a yield strength of ~ 450 MPa which decreased gradually to ~ 200 MPa at 1400°C. Increasing the silicon level to 16.5 at % (with 40 vol % $Nb_5Si_3$ phase) increased the high-temperature strengths significantly to ~ 650 MPa at 1200°C and 300 MPa at 1400°C. The room-temperature fracture toughness for the Nb-10 at % Si was ~ 20 MPa$\sqrt{m}$ while that for Nb-16.5 at %Si, it was ~ 13 MPa$\sqrt{m}$. Further, compression creep tests in vacuum at 1200°C showed (5) that for the Nb-10 at % Si alloy, the minimum rates were about 5 orders of magnitude smaller than those for the commercial Nb alloys; as an example, for the model alloy, a creep rate of ~ $10^{-8}$ $sec^{-1}$ was determined at a stress of 100 MPa and of $10^{-7}$ $sec^{-1}$ at a stress of 200 MPa. Recently, Kim et al (36) have examined the room temperature fracture toughness of Nb-Si-Mo alloys and showed that Mo addition improves the fracture toughness of Nb-Si alloys.

Additions of elements such as Ti, Al, Cr, Hf to the binary Nb-Si composition for enhancing oxidation resistance degraded the high-temperature strengths and creep resistance somewhat, while maintaining the room-temperature fracture toughness in the neighborhood of 20 MPa$\sqrt{m}$. Reasonable strength levels of ~ 150 MPa at 1200°C were still obtained. It should be mentioned

here that the maximum temperature capability of the currently used Ni-base superalloy single crystals (e.g. PW 1480) is ~ 1150°C. Therefore, an advantage of the complex Nb-base alloys would be at temperatures above 1150°C; current alloy development efforts are aimed at this high-temperature regime.

## Summary and Conclusions

This paper has briefly discussed the phase distribution observed in a wide variety of multicomponent Nb-Ti-Si base alloys that are potential candidates for high-temperature applications. In particular the kinetics, as well as the microstructural features associated with these alloys, during oxidation are elaborated. From all the experimental results, it is appears that the mechanism of oxidation of multicomponent alloys containing silicide is not changed to any extent by alloy chemistry, though the kinetics appears to be quite influenced. Clearly, oxygen diffusion into the β phase occurs rapidly, and due to the substantial solubility for oxygen even in the multicomponent alloys, alloy oxidation is quite rapid. Selective internal oxidation of alloying elements such as Hf appears to occur due to its high thermodynamic stability. Oxygen solubility in the silicide phase appears to be limited and so does oxygen diffusion. Oxygen diffusion is substantially aided by the internal defects in the alloy with the grain boundaries and phase boundaries acting as short-circuit diffusion paths. During these stages of oxidation, the kinetics of oxidation can be roughly described by a modified Wagner mechanism in which diffusion of oxygen through the oxide, as well as substantial dissolution of oxygen in the β phase, is considered. During oxidation at temperatures below approximately 900°C, the surface of the alloy, just below the adherent oxide scale, contained numerous cracks (mostly in the silicide phase) parallel to and following the contour of the sample surface. Residual stresses built up in the β phase during oxidation and cause near-surface failure at these relatively low temperatures.

## Acknowledgements

We sincerely express our appreciation to several members of our research team for assistance in experimental work as well as many useful discussions. ESKM and MGM also wish to acknowledge partial financial support under Air Force Contract No. F33615-01-C-5214.

## References

(1) Columbium metallurgy, Proceedings of a symposium, ed. D. L. Douglass and F. W. Kun ., (New York, Interscience Publishers, 1961).

(2) D. A. Prokoshkin and E. V. Vasileva, "Alloys of niobium", ed. A. M. Samarin, translated from Russian by N. Kaner ; translation edited by Molly Gleiser, (Jerusalem: Israel Program for Scientific Translations, 1965).

(3) "High-temperature Niobium Alloys", Proceedings of a symposium, eds. J. J. Stephens and I. Ahmad, (TMS, 1991).

(4) E. N. Sheftel and O. A. Bannykh, "Niobium base alloys", Proceedings of the 13th International Plansee Seminar, eds. Bildstein and R. Eck, (Metallwerk Plansee, Reutte, 1993), 43- 69.

(5) P. R. Subramanian, M. G. Mendiratta and D. M. Dimiduk, "The development of Nb-based advanced intermetallic alloys for structural applications," J. of Met., 48 (1) (1996), 33-38.

(6) E. N. Sheftel and O. A. Bannykh, "Principles of Alloying and design of structure of high-temperature high-strength niobium alloys," Tungsten and Refractory Metals-1994, eds. A. Bose and R. J. Dowding (Metals Powder Industries Federation, New Jercy, 1995), 629-655.

(7) M. R. Jackson, "Alloying concepts for Nb-base refractory metals," Tungsten and Refractory Metals-1994, eds. A. Bose and R. J. Dowding (Metals Powder Industries Federation, New Jercy, 1995), 665-672.

(8) P. R. Subramanian, M. G. Mendiratta and D. M. Dimiduk, "Development approaches for advanced intermetallic materials – Historical perspective and selected successes," Structural Intermetallics, eds. R. Darolia, J. J. Lewandowski, C. T. Liu, P. L. Martin, D. B. Miracle and M. V. Nathal, (TMS, 1993), 619-630.

(9) P. R. Subramanian, M. G. Mendiratta, D. M. Dimiduk and M. A. Stucke, "Advanced intermetallic alloys – beyond gamma titanium aluminides'" Mat. Sci. Engg., A239-240 (1997), 1-13.

(10) M. R. Jackson, "Ductile low-density alloys based on niobium," Tungsten and Refractory Metals-1994, eds. A. Bose and R. J. Dowding (Metals Powder Industries Federation, New Jercy, 1995), 65- 72.

(11) P. R. Subramanian, M. G. Mendiratta and D. M. Dimiduk, "Microstructures and mechanical behavior of Nb-Ti base beta + silicide alloys," High-temperature Silicides and Refractory Alloys, eds. C. L. Briant, J. J. Petrovic, B. P. Bewlay, A. K. Vasudevan and H. A. Lipsitt (MRS, Pittsburgh, 1994), 491-502.

(12) T. N. Rhodin, Jr., and Del. Wilmington, "Metal Production", US Patent # 2,838,396, 1958.

(13) R. C. Svedberg, R. L. Ammon, "Oxidation resistant niobium alloy – Mechanically alloying niobium intermetallic and niobium alloy", US Patent # 4,836,849, 1989.

(14) R. A. Perkins, K. T. Chiang and G. H. Meier, " Effect of alloying, rapid solidification, and surface kinetics on the high-temperature environmental resistance of niobium," (AFOSR report, LMSC-F195926, 1987).

(15) R. A. Perkins, K. T. Chiang, G. H. Meier and R. Miller, "Formation of alumina on niobium and titanium alloys," Oxidation of High-temperature Intermetallics, eds. T. Grobstein and J. Doychak (TMS, Warrendale, 1988), 157-169.

(16) R. A. Perkins, K. T. Chiang and G. H. Meier, "Formation of alumina on Nb-Al alloys', Scripta Metall., 22 (1988), 419-424.

(17) E. M. Levin, C. R. Robbins and H. F. McMurdie, Phase diagram for ceramics (The American Ceramic Society, 1964), 142-363.

(18) E. S. K. Menon, M. G. Mendiratta and D. M. Dimiduk, "High-temperature oxidation mechanisms in Nb-Silicide bearing multicomponent alloys", Structural Intermetallics 2001, eds K. J. Hemker, D. M. Dimiduk, H. Clemens, R. Darolia, H. Inui, J. M. Larsen, V. K. Sikka, M. Thomas and J. D. Whittenberger (TMS, 2001), 591-600.

(19) S. Hanada ,"Niobium aluminides", Current opinion in Solid State and Materials Science, 2 (1997), 279-283.

(20) E. S. K. Menon, P. R. Subramanian and D. M. Dimiduk, "Phase transformations in Nb-Al-Ti alloys" Met. and Mat. Trans., 27A (1996), 1647-1659.

(21) E. A. Loria, "The processing-microstructure property relationship for a multicomponent Nb-Ti-Al alloy", Mat. Sci. Engg., A271 (1999), 430-438.

(22) K. J. Leonard and V. K. Vasudevan, "Phase equilibria and solid state transformations in Nb-rich Nb-Ti-Al intermetallic alloys", Intermetallics, 8 (2000), 1257-1268.

(23) M.G. Mendiratta and D.M. Dimiduk, "Microstructures and mechanical behavior of two-phase Nb silicide – Nb alloys" Mater. Res. Soc. Symp. Proc., 133 (1989), 441-446.

(24) M.G. Mendiratta and D.M. Dimiduk, " Phase relations and transformation kinetics in the high Nb region of the Nb-Si system", Scripta Metall., 25 (1991), 237-42.

(25) M.G. Mendiratta, J.J. Lewandowski and D.M. Dimiduk, "Strength and ductile phase toughening in the two phase Nb / $Nb_5Si_3$ alloys", Met. Trans. A., 22A (1991), 1573-1583.

(26) M.G. Mendiratta and D.M. Dimiduk, " Strenght and toughness of a Nb/$Nb_5Si_3$ composite", Met. Trans. A., 24A (1993), 501-504.

(27) O. Kubaschewski and B. E. Hopkins, Oxidation of Metals and Alloys (Academic Press, Belfast, 1962), 82-87.

(28) P. Kofstad, High-temperature Oxidation of Metals (John Wiley & Sons, Inc., New York, 1966), 112-146.

(29) *Ibid*. Pages 147-227.

(30) G. H. Meier, "Fundamentals of oxidation of high-temperature intermetallics," Oxidation of High-Temperature Intermetallics, eds. T. Grobstein and J. Doychak, (TMS, Warrendale, 1988), 1-16.

(31) T. Murakami, S. Sasaki, K. Ichikawa and A. Kitahara, "Microstructure, mechanical properties and oxidation behavior of Nb-Si-Al and Nb-Si-N powder compacts prepared by spark plasma sintering", Intermetallics, 9 (2001), 621-627.

(32) T. Murakami, S. Sasaki, K. Ichikawa and A. Kitahara, "Oxidation resistance of powder compacts of the Nb-Si-Cr system and $Nb_3Si_5Al_2$ matrix compacts prepared by spark plasma sintering", Intermetallics, 9 (2001), 629-635.

(33) E. S. K. Menon, M. G. Mendiratta, T. A. Parthasarathy, Unpublished research, AFRL/MLLM (UES Inc.), Wright-Patterson AFB, OH.

(34) M. R. Jackson, US Patent 331 762 (3), 1989.

(35) M. Vilasi, M. Francois, R. Podor and J. Steinmetz, " New silicides for new niobium protective coatings", J. Alloys and Compounds, 264 (1998), 244-251.

(36) W-Y. Kim, H. Tanaka, A. Kasama, S. Hanada, "Microstructure and room temperature fracture toughness of $Nb_{ss}/Nb_5Si_3$ in situ composites", Intermetallics, 9 (2001), 827-834.